Mechanical Properties of Monolayer Graphene Oxide

Ji Won Suk, Richard D. Piner, Jinho An, and Rodney S. Ruoff*

Department of Mechanical Engineering and the Texas Materials Institute, The University of Texas at Austin, Austin, Texas 78712-0292

Revelations of the unique electronic,[1] mechanical,[2] thermal,[3–5] and optical properties[6] of graphene have put emphasis on the development of large-scale production of graphene to make graphene-based products industrially viable. We identify four methods for producing monolayer graphene in significant quantities: growth on metal substrates,[7,8] epitaxial growth on silicon carbide,[9,10] chemical reduction of graphene oxide (G−O) in colloidal suspension,[11−13] and plasma-enhanced chemical vapor deposition of graphene powder.[14] Of these methods, making colloidal suspensions of G−O is a cost-effective and easily scalable approach for obtaining graphene-like platelets through a solution-based route. G−O is a promising candidate as a component in paper-like materials,[13,15−18] polymer composites,[11] transparent conducting films,[19,20] nanomechanical devices,[21] as a compliant substrate for high-temperature processing,[22] in electrical energy storage systems,[23,24] and as discussed in several recent reviews.[25−29] There is a need for fundamental understanding of G−O and its chemical variants, including for building a reliable database of properties for applications. Although the structure of G−O has been discussed in terms of several models, detailed understanding of its structure is still being developed.[30−33] G−O consists of a hexagonal carbon network having both sp^2- and sp^3-hybridized carbons bearing hydroxyl and epoxide functional groups on its "basal" plane, whereas the edges are mostly decorated by carboxyl and carbonyl groups. Recently, a "swiss cheese" model was proposed to rationalize $I−V$ data obtained on G−O as it was being reduced in which graphene-like regions are separated by relatively heavily functionalized regions,[34] and scanning transmission electron microscopy (STEM) combined with electron energy loss spectroscopy (EELS) has proven that the functional groups in G−O are distributed in an aperiodic way.[35]

The mechanical properties of graphene and reduced graphene oxide have been investigated with both experimental and theoretical approaches. Lee *et al.* reported the Young's modulus of ~1.0 TPa and the ultimate breaking strength of ~130 GPa by indenting the center of a series of monolayer graphene membranes with a diamond-coated tip using atomic force microscopy (AFM).[2] Gomez-Navarro *et al.* reported a Young's modulus of 0.25 ± 0.15 TPa for a chemically reduced monolayer graphene oxide beam by AFM nanoindentation.[36] Theoretically, Paci *et al.* showed that oxidation process significantly decreases the in-plane Young's modulus and fracture strength of graphite oxide by using a Monte Carlo-based scheme and molecular dynamics simulations.[37] However, to the best of our knowledge, the mechanical

ABSTRACT Mechanical properties of ultrathin membranes consisting of one layer, two overlapped layers, and three overlapped layers of graphene oxide platelets were investigated by atomic force microscopy (AFM) imaging in contact mode. In order to evaluate both the elastic modulus and prestress of thin membranes, the AFM measurement was combined with the finite element method (FEM) in a new approach for evaluating the mechanics of ultrathin membranes. Monolayer graphene oxide was found to have a lower effective Young's modulus (207.6 ± 23.4 GPa when a thickness of 0.7 nm is used) as compared to the value reported for "pristine" graphene. The prestress (39.7−76.8 MPa) of the graphene oxide membranes obtained by solution-based deposition was found to be 1 order of magnitude lower than that obtained by others for mechanically cleaved graphene. The novel AFM imaging and FEM-based mapping methods presented here are of general utility for obtaining the elastic modulus and prestress of thin membranes.

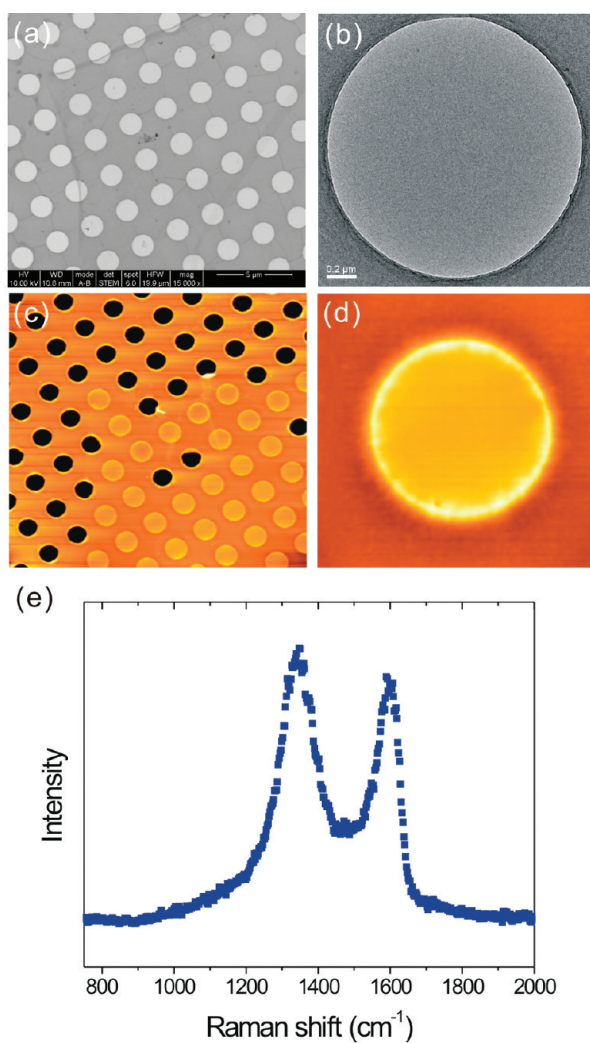**KEYWORDS:** graphene oxide · mechanical properties · membranes · atomic force microscopy · finite element analysis

Figure 1. G—O platelet covering open holes. (a) STEM image. (b) TEM image. (c) AFM topology image in 20 × 20 μm² scanned area. (d) AFM topology image in 2.2 × 2.2 μm². (e) Raman spectrum obtained from one individual G—O membrane with a 532 nm wavelength incident laser.

properties of monolayer G—O platelets have not yet been reported.

In this paper, AFM imaging in contact mode was used to extract the mechanical properties of nanometer-thick membranes consisting of one layer, two overlapped layers, and three overlapped layers of G—O platelets. The effective Young's modulus and prestress were obtained by using a mapping method based on the finite element method (FEM). The measurement and analysis techniques enable us to obtain both the elastic modulus and prestress of ultrathin membranes simultaneously.

RESULTS AND DISCUSSION

An aqueous dispersion of G—O platelets (graphite oxide was made by the modified Hummers method[38]) was made by slow stirring in ultrapure water. It was diluted and deposited over a carbon film TEM grid (QUANTIFOIL holey carbon film grid; QUANTIFOIL Micro Tools

GmbH). One droplet of the solution was dropped on the grid and dried in air, yielding well-distributed G—O platelets. Figure 1 shows G—O platelets over regions of these holey carbon film grids. STEM (Quanta F600 ESEM, FEI) and AFM (model CP, Park Scientific Instruments) topology images indicate that the G—O film regions span over several holes in the grid (Figure 1a,c). Each hole has a 1.30 μm (or 1.75 μm, for a different grid) diameter and a 2.50 μm center-to-center spacing, indicating that the local regions of the G—O films spanned tens of micrometers in lateral dimension, which allowed easy identification of individual membranes not having any wrinkles or folds. Most of the membranes survived the deposition process. Transmission electron microscopy (TEM; 2010F, JEOL) and AFM topology images of one representative membrane show a clean and wrinkle-free membrane over a hole (Figure 1b,d). The Raman spectrum (WITec alpha300, a laser wavelength of 532 nm, 100× objective lens) shows D and G bands, as expected (Figure 1e).[39] The circular shape of the membranes provides a well-defined sample geometry and thus boundary conditions such that no particular stress concentration is expected around the circumference. The through-hole configuration allowed use of TEM to observe the same membranes that AFM measurements were performed on.

AFM has been used for characterizing the mechanical properties of micro/nanostructures including microcantilevers,[40] nanowires,[41−43] thin films,[44] and biological materials[45−47] by obtaining force—distance curves.[48] However, the standard force—distance measurement suffers from instabilities due to the discontinuous motion of the AFM tip ("jumping" or "snapping").[49] In addition, there is uncertainty in the exact position of the probe on the sample, and this is made worse by the fact that the tip slides across the sample during the measurement. These factors adversely affect reliability and reproducibility. Instead of using the conventional method, other researchers have used contact mode scanning AFM to characterize the mechanical properties of SiC nanorods and carbon nanotubes by bending these structures and using the lateral force detector to measure the bending force, while using the image to measure the displacement.[50] Recently, contact scanning mode AFM was used for mechanical testing of freestanding microcantilevers to overcome the intrinsic drawbacks of the conventional force—distance method including nonlinearities of the photodetector.[51]

AFM imaging in contact mode was used to measure the mechanical deformation of G—O membranes. The principle of the AFM measurement is illustrated in Figure 2a. When the AFM tip scans over a membrane (or any suspended structure) with a constant normal force, the membrane can mechanically deform along a scanned line (the dashed lines in Figure 2a). By recording the tip displacement, topology images can be obtained at different normal forces. The image is not a true topology map, but a

map of the tip trajectory as it was scanned over the membrane (the solid line in Figure 2a). This imaging method has the tip in contact with the sample, which provides several advantages compared with the conventional force−distance method: (i) it avoids the relatively large loads applied with traditional force−distance experiments as built into most commercial AFMs; (ii) it provides a stable and continuous measurement by eliminating instability due to jumping or snapping of the AFM tip; (iii) it allows one to extract the force−distance relationships at every point on the sample with good lateral resolution (*i.e.*, without doubt about the precise position of the probe); and (iv) it allows for the use of a relatively flexible supporting substrate by measuring deformation of the suspended sample relative to any potential deformation of the supporting substrate; this was useful here as the QUANTIFOIL substrate allowed for relatively trivial acquisition of TEM data of the same membranes.

The elastic modulus and prestress are important parameters in micro/nanoscale devices for determining deformation, resonant frequency, and quality factor. If the membrane is under tensile stress at zero load, it is stiffer, which means less mechanical deformation and increased resonant frequency. FEM was used with a mapping technique for the evaluation of elastic modulus and prestress. Figure 2b shows an illustration of a three-dimensional (3D) map plotting the displacement difference ($\Delta d = d_{FEM} - d_{measured}$) between the FEM calculated (d_{FEM}) and experimentally measured ($d_{measured}$) displacements, for a given elastic modulus and a prestress. For a given load and measured displacement, the solution to the problem is under-specified, thus there are an infinite number of solutions. When the calculated displacement by FEM is the same as the experimentally measured one ($\Delta d = 0$), these solutions can be plotted as a line as shown in Figure 2c. However, a different load leads to a different set of solutions, resulting in another line. If multiple data sets are plotted, the intersection of the lines provides the correct values of the elastic modulus and the prestress (Figure 2c).

The mechanical deformation of the G−O membranes was obtained by scanning the whole membrane with several different loads from the AFM tip (MLCT cantilever A, calibrated by resonance frequency measurement,[52] Veeco Instruments) in contact mode. Panels a and b of Figure 3 show that the 3D AFM topology images are at two different forces, 0 and 2.65 nN, respectively. The high ridges at the edge of the membrane are a consequence of the shape of the perforated QUANTIFOIL grids. The lateral size of individual G−O platelets is on the order of tens of micrometers, thus having huge surface areas compared to the individual membrane areas, so adhesion forces (van der Waals forces) are large enough to provide good clamping of the membranes for the forces applied in these measure-
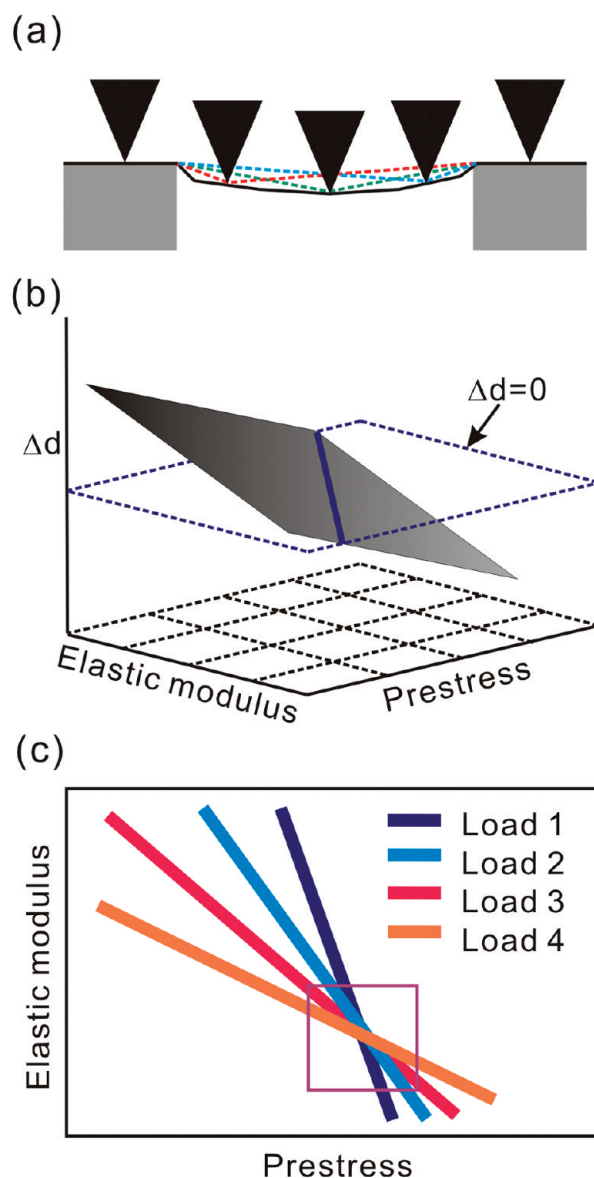

Figure 2. Illustration of contact mode AFM imaging and FEM-based mapping. (a) AFM tip at different positions on a sample (the dashed lines represent (schematically) the deformed shape of the membrane at that contact point). The solid line represents the acquired tip trajectory, which corresponds to the obtained AFM topology image. (b) Three-dimensional map of displacement difference ($\Delta d = d_{FEM} - d_{measured}$) from the obtained membrane deformation at one load condition. (c) Two-dimensional map of possible combinations of elastic moduli and prestresses obtained using four different normal force loads (Load 1 < Load 2 < Load 3 < Load 4).

ments. To test whether slipping is occurring, AFM measurements were repeatedly made on one membrane (specifically, apply 0 nN to higher forces, break the contact, and then repeat, 3 times). Force−distance curves from each of these three measurements were very close to each other, showing that there was no slippage in the measurements (Figure S1 in Supporting Information). It is well-known that the amount of water molecules trapped between stacked G−O platelets depends on the relative humidity. This could conceivably
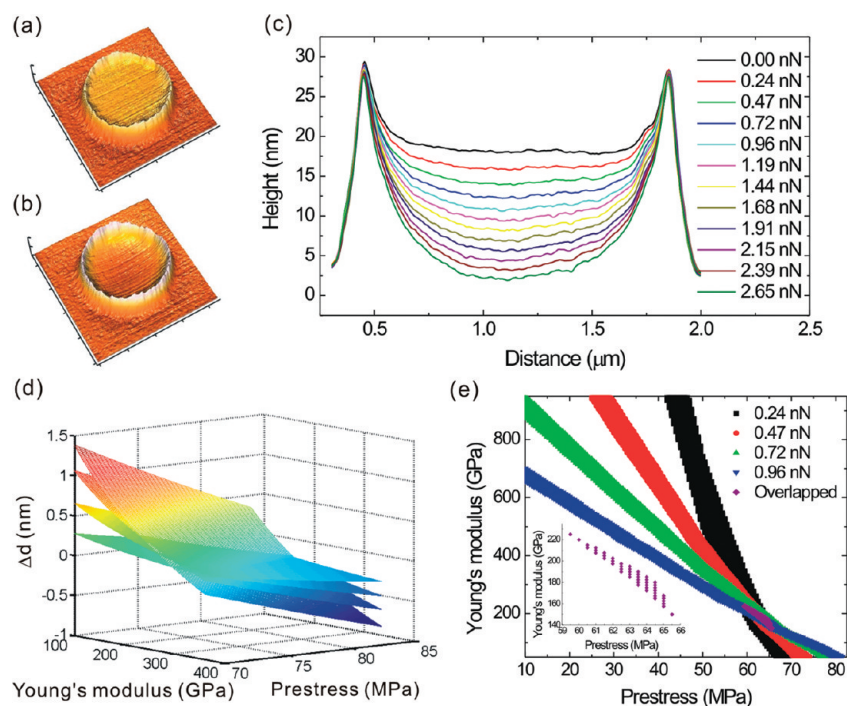
Figure 3. Measurements of deformation *versus* load and analysis of G—O membranes. (a,b) Three-dimensional AFM images of one membrane at two different loads of 0 and 2.65 nN. (c) Cross-sectional profile of a scanned membrane at varying normal loads shows the increased deflection of the membrane with increasing applied force. (d) Three-dimensional map of the displacement difference ($\Delta d = d_{FEM} - d_{measured}$) at four different load conditions of 0.24, 0.47, 0.72, and 0.96 nN. (e) Two-dimensional elastic modulus *vs* prestress map obtained from four different normal force loads. The inset shows the overlapped area of the most probable values of the Young's modulus and prestress.

alter the interaction forces between adjacent G—O layers. To avoid variations in interlamellar water content, all measurements were done at a nearly constant relative humidity. The reader is also referred to a recent modeling study of the mechanics of graphene oxide paper.[53]

Cross-section profiles across the center of the holes were taken to obtain deformation profiles and averaged with five scanning lines for a total width of approximately 30 nm (Figure 3c). The averaged cross-section profile taken at 0 nN was subtracted from those at each subsequent load in Figure 3c. The difference between cross-section profiles corresponds to the amount that the membrane deflects at a given load. This deflection is modeled as a flat circular membrane under normal load. The displacement values at the center of the membrane from the height difference profiles were obtained and are equivalent to the values of a force—distance curve. The conventional force—distance method in AFM requires a zero displacement reference from a rigid substrate. The AFM imaging method presented here, however, enables us to extract force—distance relationships even with a relatively flexible substrate by measuring the relative displacement of membrane relative to such a substrate at different loads.

Numerical calculation was performed with ANSYS 11.0 by modeling the contact between the AFM tip and the membrane. Graphene can be modeled as a

two-dimensional (2D) membrane with no bending stiffness.[2] However, the addition of oxygen atoms in G—O induces a local bonding reinforcement, which was reported to increase the elastic bending coefficient.[54] Thus, the bending stiffness was considered in the analysis of G—O membranes. Figure 3d shows one example of a 3D map of the displacement differences (Δd) at four different loads. The 2D elastic modulus *versus* prestress map was then obtained by intersecting with a plane at $\Delta d = 0$ from the 3D map (Figure 3e). The overlapped area corresponds to the most likely values of the Young's modulus and prestress of the measured membrane.

Monolayer graphene is a "perfect" 2D material, so its mechanical behavior under tensile loading has been described by a 2D elastic constant E^{2D} with units of force/length.[2] For the purpose of comparison, the effective Young's modulus of G—O was converted to E^{2D} (elastic stiffness = Young's modulus × thickness) by considering its thickness (0.7 nm as measured by AFM on mica).[55] Selected area electron diffraction (SAED) patterns were obtained in TEM for the same membranes where AFM measurement was done to obtain their thickness by measurement of the number of layers (see Supporting Information for details). In this manner, membranes consisting of one layer, two overlapped layers, and three overlapped layers of G—O platelets were studied. When the thickness of G—O platelets was evaluated on mica with AFM, every plate-
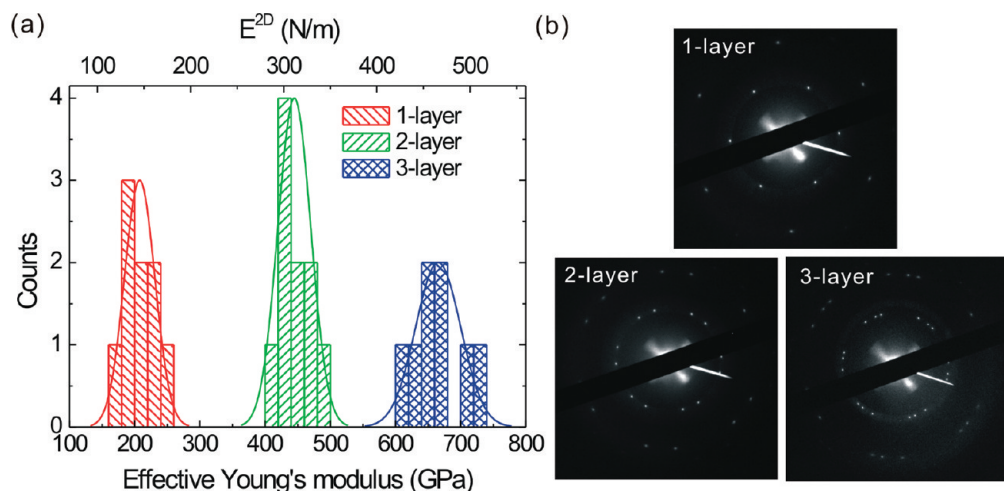
Figure 4. (a) Histogram of the effective Young's modulus of G—O platelet membranes with thickness assumed to be one layer for all measured membranes. The 2D elastic constant E^{2D} is also calculated from the assumed monolayer thickness. Nine, ten, and eight G—O membranes (composed of one layer, two overlapped layers, and three overlapped layers, respectively) were measured. The solid lines represent Gaussian fits to the data. (b) SAED patterns from G—O membranes composed of one layer, two overlapped layers, and three overlapped layers.

let showed monolayer thickness. Therefore, it is assumed that all G—O platelets were monolayer at the outset of our work. This is also consistent with SAED observations. The G—O platelet having a single hexagonal pattern shows stronger intensity for the inner {100} spot pattern than the outer {110} spot pattern (Figure 4b). This is consistent with what was reported for monolayer G—O diffraction spot intensities in earlier work.[56] Combined with AFM results, we can conclude that the G—O platelets studied in this work are one layer, two overlapped layers, and three overlapped layers of G—O platelets that had been fully exfoliated into single sheets during the exfoliation process and that have overlapped onto the TEM grids during the dry down process.

First, all measured membranes were analyzed by assuming them to be a monolayer, which means 0.7 nm was used for the thickness. As shown in Figure 4a, the effective Young's moduli were "binned" into three groups, which correspond to the number of layers of the membranes. The monolayer G—O membranes have an effective Young's modulus of 207.6 ± 23.4 GPa ($E^{2D} = 145.3 \pm 16.4$ N/m). Monolayer graphene obtained from mechanically cleaved graphite has a measured Young's modulus of ~1.0 TPa, corresponding to $E^{2D} = 342 \pm 30$ N/m.[2] Therefore, E^{2D} of the G—O monolayer platelets studied here is about half that of graphene. If a zero bending stiffness is assumed for monolayer G—O, as is the case for graphene, the effective Young's modulus is 156.5 ± 23.9 GPa ($E^{2D} = 109.6 \pm 16.7$ N/m), as shown in Figure S7 in Supporting Information.

During the oxidation process, the original sp^2-bonded carbon atoms of graphene were modified into sp^3-bonded atoms *via* bonding with oxygen. It has been reported that the fraction of sp^3-bonded carbon is

about 40% in G—O with a measured O/C ratio of 1:5 by using STEM combined with EELS.[35] *Ab initio* calculations[35] support this picture, but the ratio determined by elemental analysis can be as low as 1:2. In Figure 4b, the SAED patterns we acquired consist of white rings with clear graphene diffraction patterns, which qualitatively shows that G—O platelets have aperiodic "decoration" of the basal plane by functional groups. Paci *et al.* calculated mechanical properties of pristine graphene and G—O using a Monte Carlo-based scheme and molecular dynamics simulations.[37] In their work, the stress—strain curve of pristine graphene was compared with that of G—O having a hole using the same thickness (0.34 nm) as pristine graphene. The hole in G—O is one hexagonal unit, that is, six missing C atoms in a unit cell containing 128 C atoms that is repeated through periodic boundary conditions. The calculated stress—strain curve of G—O with such a hole had a slope about one-half that of ideal graphene, and its fracture strength was about one-third of ideal graphene (Figure 8 in ref 37). High-resolution TEM observations show that reduced G—O platelets do have (even quite large) holes.[57]

For two-layer and three-layer G—O membranes, the effective Young's moduli are 444.8 ± 25.3 and 665.5 ± 34.6 GPa, respectively, if it is assumed that the membrane is a monolayer. Thus, the effective Young's moduli of two-layer and three-layer membranes accounting for the real thickness are 223.9 ± 17.7 GPa ($E^{2D} = 156.7 \pm 12.4$ N/m) and 229.5 ± 27.0 GPa ($E^{2D} = 160.7 \pm 18.9$ N/m), respectively (Figure S5 in Supporting Information). The close similarity between values for one layer, two overlapped layers, and three overlapped layers of G—O platelets as membranes indicates that the bonding between layers in the two-layer and three-layer membranes is strong enough to avoid any inter-
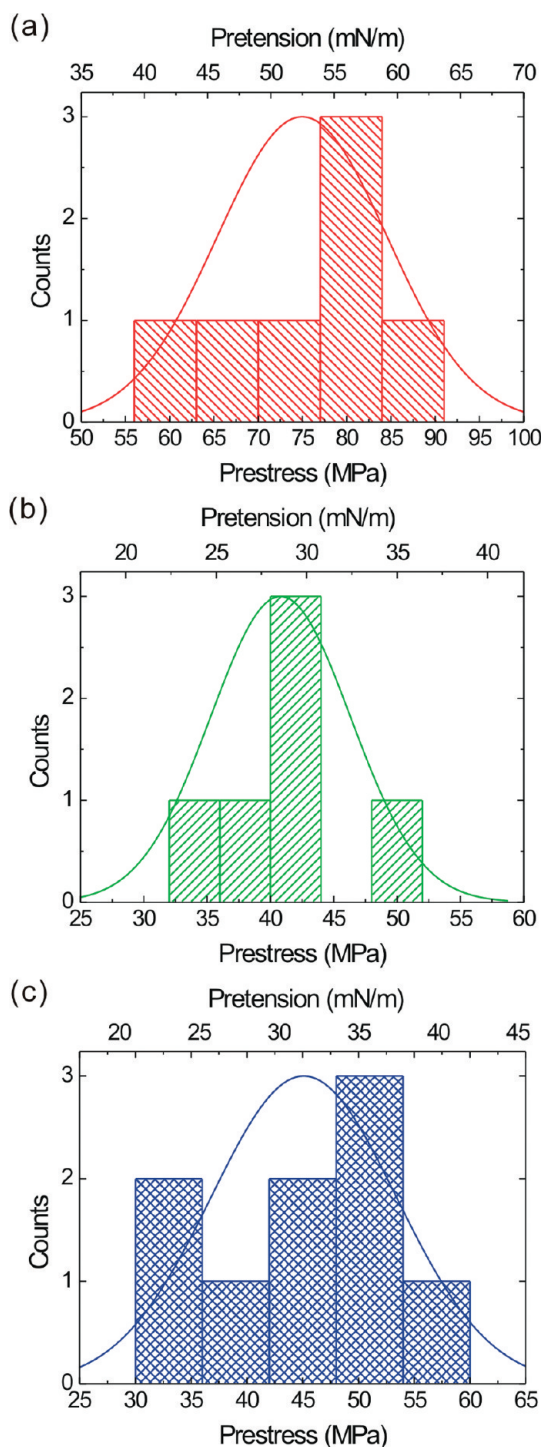
Figure 5. Histograms of prestresses of G—O membranes composed of (a) one layer, (b) two overlapped layers, and (c) three overlapped layers. Each prestress was analyzed using the appropriate overall membrane thickness. The solid lines represent Gaussian fits to the data.

layer sliding (for the forces and resulting deformations arising from these measurements). Indeed, "graphene oxide paper" consisting of overlapped and stacked G—O platelets typically fractured at strains of about 0.4%, and recent modeling[53] shows that the H-bonding responsible for the mechanics of such stacked G—O platelets would not be at all disrupted by the small strains applied here. For example, for the 1.30 or 1.75 μm diameter membranes here were, at maximum deflection, only deformed 15 to 30 nm out of plane.

Figure 5 shows prestresses of G—O membranes composed of one layer, two overlapped layers, and three overlapped layers as 76.8 ± 19.9, 45.4 ± 8.1, and 39.7 ± 5.5 MPa, respectively, which correspond to pretensions of 53.8 ± 13.9, 31.8 ± 6.1, and 27.8 ± 3.9 mN/m. The mechanically cleaved graphene samples studied by others had a broad distribution of pretension values of 70—740 mN/m,[2] or about 1 order of magnitude higher than that of the G—O membranes. This suggests that the solution-based deposition method yields a smaller and also relatively constant prestress on the different membranes, while mechanical rubbing yields a broader range of values with much larger "high end" values. In this respect, perhaps the solution-based approach will allow for configuring devices with mechanical response closer to the inherent mechanical properties of the membranes.

CONCLUSION

In conclusion, we have developed and used a new contact mode AFM imaging method combined with finite element analysis to obtain the mechanical properties of G—O membranes composed of one layer, two overlapped layers, and three overlapped layers. This method involves recording topology images at different normal loads on a given membrane and FEM-based mapping to obtain the elastic modulus and the prestress of thin membranes. The individual (*i.e.*, 1 layer) platelets of G—O had an effective Young's modulus and prestress of 207.6 ± 23.4 GPa and 76.8 ± 19.9 MPa (for an assigned 0.7 nm thickness), respectively. The solution-based approach to fabricate membranes provided 1 order of magnitude lower prestress compared to that of mechanically exfoliated graphene reported by others.[2] This work demonstrates direct mechanical measurements on membranes composed of G—O platelets as well as the potential for "universal use" of this new measurement and analysis method to obtain the elastic modulus and prestress of ultrathin membranes.

METHODS

AFM Imaging. All AFM measurements were done at 512×512 resolution and a scanning rate of 1 Hz in a 2.2×2.2 μm² scan. A 1/F filter was applied to reduce the background noise in the data. After obtaining the cross-section profiles (Figure 3c), 20 points (cor-

responding to ~110 nm width) at the center of the cross-section profile were averaged and used for the analysis. The thickness of G—O platelets was measured by AFM after depositing them on mica.[58] A thickness of 0.7 nm is used for all analysis. All measurements were conducted at a nearly constant humidity of 35—40%.

FEM Analysis. The ANSYS Parametric Design Language (APDL) was used to model the contact between the AFM tip and the membrane with varying assumed values of elastic moduli and prestresses. Simulations were done with a 1.30 μm (or 1.75 μm) diameter membrane with an assumed thickness of 0.7 nm. A 2-node shell element was used for axisymmetric analysis of the membrane. We modeled the AFM tip as a hemisphere with a radius of 23.9 nm (see Supporting Information) and used material properties of silicon nitride for the AFM tip. The contact between the tip and membrane was assumed to be frictionless. The membrane was assumed to be isotropic. The Poisson's ratio of the G—O membrane was assumed to be 0.165, the value for graphite in the basal plane.[2,59] Displacements at the center of the membrane were calculated at 10 GPa and 2 MPa increments for elastic moduli and prestresses, respectively. Each calculated displacement was compared with one measured displacement at a given force. In order to reduce computing time by assuming linear behavior between neighboring calculated data points, a linear interpolation was done for each pair of neighboring data points, and five interpolated points were thereby obtained. On the basis of the calculations and comparisons with the measured displacements at four different forces, 3D and 2D maps were constructed as shown in Figure 4d,e, respectively. The effective Young's modulus was obtained by averaging all of the calculated values in the overlapped region of the 2D map.

Supporting Information Available: Details about experiments and analysis. This material is available free of charge *via* the Internet at http://pubs.acs.org.

REFERENCES AND NOTES

1. Bolotin, K. I.; Sikes, K. J.; Jiang, Z.; Klima, M.; Fudenberg, G.; Hone, J.; Kim, P.; Stormer, H. L. Ultrahigh Electron Mobility in Suspended Graphene. *Solid State Commun.* **2008**, *146*, 351–355.

2. Lee, C.; Wei, X. D.; Kysar, J. W.; Hone, J. Measurement of the Elastic Properties and Intrinsic Strength of Monolayer Graphene. *Science* **2008**, *321*, 385–388.

3. Seol, J. H.; Jo, I.; Moore, A. L.; Lindsay, L.; Aitken, Z. H.; Pettes, M. T.; Li, X. S.; Yao, Z.; Huang, R.; Broido, D.; *et al.* Two-Dimensional Phonon Transport in Supported Graphene. *Science* **2010**, *328*, 213–216.

4. Cai, W.; Moore, A. L.; Zhu, Y.; Li, X.; Chen, S.; Shi, L.; Ruoff, R. S. Thermal Transport in Suspended and Supported Monolayer Graphene Grown by Chemical Vapor Deposition. *Nano Lett.* **2010**, *10*, 1645–1651.

5. Balandin, A. A.; Ghosh, S.; Bao, W. Z.; Calizo, I.; Teweldebrhan, D.; Miao, F.; Lau, C. N. Superior Thermal Conductivity of Single-Layer Graphene. *Nano Lett.* **2008**, *8*, 902–907.

6. Nair, R. R.; Blake, P.; Grigorenko, A. N.; Novoselov, K. S.; Booth, T. J.; Stauber, T.; Peres, N. M. R.; Geim, A. K. Fine Structure Constant Defines Visual Transparency of Graphene. *Science* **2008**, *320*, 1308.

7. Li, X.; Cai, W.; An, J.; Kim, S.; Nah, J.; Yang, D.; Piner, R.; Velamakanni, A.; Jung, I.; Tutuc, E.; *et al.* Large-Area Synthesis of High-Quality and Uniform Graphene Films on Copper Foils. *Science* **2009**, *324*, 1312–1314.

8. Kim, K. S.; Zhao, Y.; Jang, H.; Lee, S. Y.; Kim, J. M.; Kim, K. S.; Ahn, J. H.; Kim, P.; Choi, J. Y.; Hong, B. H. Large-Scale Pattern Growth of Graphene Films for Stretchable Transparent Electrodes. *Nature* **2009**, *457*, 706–710.

9. Berger, C.; Song, Z. M.; Li, X. B.; Wu, X. S.; Brown, N.; Naud, C.; Mayou, D.; Li, T. B.; Hass, J.; Marchenkov, A. N.; *et al.* Electronic Confinement and Coherence in Patterned Epitaxial Graphene. *Science* **2006**, *312*, 1191–1196.

10. Ohta, T.; Bostwick, A.; Seyller, T.; Horn, K.; Rotenberg, E. Controlling the Electronic Structure of Bilayer Graphene. *Science* **2006**, *313*, 951–954.

11. Stankovich, S.; Dikin, D. A.; Dommett, G. H. B.; Kohlhaas, K. M.; Zimney, E. J.; Stach, E. A.; Piner, R. D.; Nguyen, S. T.; Ruoff, R. S. Graphene-Based Composite Materials. *Nature* **2006**, *442*, 282–286.

12. Stankovich, S.; Piner, R. D.; Chen, X. Q.; Wu, N. Q.; Nguyen, S. T.; Ruoff, R. S. Stable Aqueous Dispersions of Graphitic Nanoplatelets *via* the Reduction of Exfoliated Graphite Oxide in the Presence of Poly(sodium 4-styrenesulfonate). *J. Mater. Chem.* **2006**, *16*, 155–158.

13. Dikin, D. A.; Stankovich, S.; Zimney, E. J.; Piner, R. D.; Dommett, G. H. B.; Evmenenko, G.; Nguyen, S. T.; Ruoff, R. S. Preparation and Characterization of Graphene Oxide Paper. *Nature* **2007**, *448*, 457–460.

14. Dato, A.; Radmilovic, V.; Lee, Z. H.; Phillips, J.; Frenklach, M. Substrate-Free Gas-Phase Synthesis of Graphene Sheets. *Nano Lett.* **2008**, *8*, 2012–2016.

15. Park, S.; Lee, K. S.; Bozoklu, G.; Cai, W.; Nguyen, S. T.; Ruoff, R. S. Graphene Oxide Papers Modified by Divalent Ions—Enhancing Mechanical Properties *via* Chemical Cross-Linking. *ACS Nano* **2008**, *2*, 572–578.

16. Park, S.; An, J.; Suk, J. W.; Ruoff, R. S. Graphene-Based Actuators. *Small* **2010**, *6*, 210–212.

17. Park, S.; Mohanty, N.; Suk, J. W.; Nagaraja, A.; An, J.; Piner, R. D.; Cai, W.; Dreyer, D. R.; Berry, V.; Ruoff, R. S. Biocompatible, Robust Free-Standing Paper Composed of a TWEEN/Graphene Composite. *Adv. Mater.* **2010**, *22*, 1736–1740.

18. Dua, V.; Surwade, S. P.; Ammu, S.; Agnihotra, S. R.; Jain, S.; Roberts, K. E.; Park, S.; Ruoff, R. S.; Manohar, S. K. All-Organic Vapor Sensor Using Inkjet-Printed Reduced Graphene Oxide. *Angew. Chem., Int. Ed.* **2010**, *49*, 2154–2157.

19. Eda, G.; Lin, Y. Y.; Miller, S.; Chen, C. W.; Su, W. F.; Chhowalla, M. Transparent and Conducting Electrodes for Organic Electronics from Reduced Graphene Oxide. *Appl. Phys. Lett.* **2008**, *92*, 233305.

20. Becerril, H. A.; Mao, J.; Liu, Z.; Stoltenberg, R. M.; Bao, Z.; Chen, Y. Evaluation of Solution-Processed Reduced Graphene Oxide Films as Transparent Conductors. *ACS Nano* **2008**, *2*, 463–470.

21. Robinson, J. T.; Zalalutdinov, M.; Baldwin, J. W.; Snow, E. S.; Wei, Z. Q.; Sheehan, P.; Houston, B. H. Wafer-Scale Reduced Graphene Oxide Films for Nanomechanical Devices. *Nano Lett.* **2008**, *8*, 3441–3445.

22. Lee, D. H.; Kim, J. E.; Han, T. H.; Hwang, J. W.; Jeon, S.; Choi, S. Y.; Hong, S. H.; Lee, W. J.; Ruoff, R. S.; Kim, S. O. Versatile Carbon Hybrid Films Composed of Vertical Carbon Nanotubes Grown on Mechanically Compliant Graphene Films. *Adv. Mater.* **2010**, *22*, 1247–1252.

23. Stoller, M. D.; Park, S.; Zhu, Y.; An, J.; Ruoff, R. S. Graphene-Based Ultracapacitors. *Nano Lett.* **2008**, *8*, 3498–3502.

24. Lee, J. K.; Smith, K. B.; Hayner, C. M.; Kung, H. H. Silicon Nanoparticles-Graphene Paper Composites for Li Ion Battery Anodes. *Chem. Commun.* **2010**, *46*, 2025–2027.

25. Park, S.; Ruoff, R. S. Chemical Methods for the Production of Graphenes. *Nat. Nanotechnol.* **2009**, *4*, 217–224.

26. Dreyer, D. R.; Park, S.; Bielawski, C. W.; Ruoff, R. S. The Chemistry of Graphene Oxide. *Chem. Soc. Rev.* **2010**, *39*, 228–240.

27. Zhu, Y.; Murali, S.; Cai, W.; Li, X.; Suk, J. W.; Potts, J. R.; Ruoff, R. S. Graphene and Graphene Oxide: Synthesis, Properties, and Applications. *Adv. Mater.* **2010**, *22*, 3906–3924.

28. Compton, O. C.; Nguyen, S. T. Graphene Oxide, Highly Reduced Graphene Oxide, and Graphene: Versatile Building Blocks for Carbon-Based Materials. *Small* **2010**, *6*, 711–723.

29. Rao, C. N. R.; Sood, A. K.; Subrahmanyam, K. S.; Govindaraj, A. Graphene: The New Two-Dimensional Nanomaterial. *Angew. Chem., Int. Ed.* **2009**, *48*, 7752–7777.

30. Scholz, W.; Boehm, H. P. Graphite Oxide. 6. Structure of Graphite Oxide. *Anorg. Allg. Chem.* **1969**, *369*, 327–340.

31. Nakajima, T.; Mabuchi, A.; Hagiwara, R. A New Structure Model of Graphite Oxide. *Carbon* **1988**, *26*, 357–361.

32. Lerf, A.; He, H. Y.; Forster, M.; Klinowski, J. Structure of Graphite Oxide Revisited. *J. Phys. Chem. B* **1998**, *102*, 4477–4482.

33. Cai, W.; Piner, R. D.; Stadermann, F. J.; Park, S.; Shaibat, M. A.; Ishii, Y.; Yang, D.; Velamakanni, A.; An, S. J.; Stoller, M.; *et al.* Synthesis and Solid-State NMR Structural Characterization of ^{13}C-Labeled Graphite Oxide. *Science* **2008**, *321*, 1815–1817.

34. Jung, I.; Dikin, D. A.; Piner, R. D.; Ruoff, R. S. Tunable Electrical Conductivity of Individual Graphene Oxide Sheets Reduced at "Low" Temperatures. *Nano Lett.* **2008**, *8*, 4283–4287.

35. Mkhoyan, K. A.; Contryman, A. W.; Silcox, J.; Stewart, D. A.; Eda, G.; Mattevi, C.; Miller, S.; Chhowalla, M. Atomic and Electronic Structure of Graphene-Oxide. *Nano Lett.* **2009**, *9*, 1058–1063.

36. Gomez-Navarro, C.; Burghard, M.; Kern, K. Elastic Properties of Chemically Derived Single Graphene Sheets. *Nano Lett.* **2008**, *8*, 2045–2049.

37. Paci, J. T.; Belytschko, T.; Schatz, G. C. Computational Studies of the Structure, Behavior upon Heating, and Mechanical Properties of Graphite Oxide. *J. Phys. Chem. C* **2007**, *111*, 18099–18111.

38. Hummers, W. S.; Offeman, R. E. Preparation of Graphite Oxide. *J. Am. Chem. Soc.* **1958**, *80*, 1339.

39. Kudin, K. N.; Ozbas, B.; Schniepp, H. C.; Prud'homme, R. K.; Aksay, I. A.; Car, R. Raman Spectra of Graphite Oxide and Functionalized Graphene Sheets. *Nano Lett.* **2008**, *8*, 36–41.

40. Serre, C.; Gorostiza, P.; Perez-Rodriguez, A.; Sanz, F.; Morante, J. R. Measurement of Micromechanical Properties of Polysilicon Microstructures with an Atomic Force Microscope. *Sens. Actuators, A* **1998**, *67*, 215–219.

41. Ni, H.; Li, X. D.; Gao, H. S. Elastic Modulus of Amorphous SiO_2 Nanowires. *Appl. Phys. Lett.* **2006**, *88*, 043108.

42. Heidelberg, A.; Ngo, L. T.; Wu, B.; Phillips, M. A.; Sharma, S.; Kamins, T. I.; Sader, J. E.; Boland, J. J. A Generalized Description of the Elastic Properties of Nanowires. *Nano Lett.* **2006**, *6*, 1101–1106.

43. Zhang, H.; Tang, J.; Zhang, L.; An, B.; Qin, L. C. Atomic Force Microscopy Measurement of the Young's Modulus and Hardness of Single LaB_6 Nanowires. *Appl. Phys. Lett.* **2008**, *92*, 173121.

44. Cappella, B.; Silbernagl, D. Nanomechanical Properties of Polymer Thin Films Measured by Force-Distance Curves. *Thin Solid Films* **2008**, *516*, 1952–1960.

45. Siitonen, A. M.; Sumitomo, K.; Ramanujan, C. S.; Shinozaki, Y.; Kasai, N.; Furukawa, K.; Ryan, J. F.; Torimitsu, K. Elastic Modulus of Suspended Purple Membrane Measured by Atomic Force Microscopy. *Appl. Surf. Sci.* **2008**, *254*, 7877–7880.

46. A-Hassan, E.; Heinz, W. F.; Antonik, M. D.; D'Costa, N. P.; Nageswaran, S.; Schoenenberger, C. A.; Hoh, J. H. Relative Microelastic Mapping of Living Cells by Atomic Force Microscopy. *Biophys. J.* **1998**, *74*, 1564–1578.

47. Tao, N. J.; Lindsay, S. M.; Lees, S. Measuring the Microelastic Properties of Biological-Material. *Biophys. J.* **1992**, *63*, 1165–1169.

48. Cappella, B.; Dietler, G. Force-Distance Curves by Atomic Force Microscopy. *Surf. Sci. Rep.* **1999**, *34*, 1–104.

49. Joyce, S. A.; Houston, J. E. A New Force Sensor Incorporating Force-Feedback Control for Interfacial Force Microscopy. *Rev. Sci. Instrum.* **1991**, *62*, 710–715.

50. Wong, E. W.; Sheehan, P. E.; Lieber, C. M. Nanobeam Mechanics: Elasticity, Strength, and Toughness of Nanorods and Nanotubes. *Science* **1997**, *277*, 1971–1975.

51. Ryan, P. J.; Adams, G. G.; McGruer, N. E.; Muftu, S. Contact Scanning Mode AFM for Nanomechanical Testing of Free-Standing Structures. *J. Micromech. Microeng.* **2006**, *16*, 1040–1046.

52. Sader, J. E.; Pacifico, J.; Green, C. P.; Mulvaney, P. General Scaling Law for Stiffness Measurement of Small Bodies with Applications to the Atomic Force Microscope. *J. Appl. Phys.* **2005**, *97*, 124903.

53. Medhekar, N. V.; Ramasubramaniam, A.; Ruoff, R. S.; Shenoy, V. B. Hydrogen Bond Networks in Graphene Oxide Composite Paper: Structure and Mechanical Properties. *ACS Nano* **2010**, *4*, 2300–2306.

54. Incze, A.; Pasturel, A.; Peyla, P. Mechanical Properties of Graphite Oxides: *Ab Initio* Simulations and Continuum Theory. *Phys. Rev. B* **2004**, *70*, 212103.

55. Huang, Y.; Wu, J.; Hwang, K. C. Thickness of Graphene and Single-Wall Carbon Nanotubes. *Phys. Rev. B* **2006**, *74*, 245413.

56. Wilson, N. R.; Pandey, P. A.; Beanland, R.; Young, R. J.; Kinloch, I. A.; Gong, L.; Liu, Z.; Suenaga, K.; Rourke, J. P.; York, S. J.; *et al.* Graphene Oxide: Structural Analysis and Application as a Highly Transparent Support for Electron Microscopy. *ACS Nano* **2009**, *3*, 2547–2556.

57. Gomez-Navarro, C.; Meyer, J. C.; Sundaram, R. S.; Chuvilin, A.; Kurasch, S.; Burghard, M.; Kern, K.; Kaiser, U. Atomic Structure of Reduced Graphene Oxide. *Nano Lett.* **2010**, *10*, 1144–1148.

58. Stankovich, S.; Dikin, D. A.; Piner, R. D.; Kohlhaas, K. A.; Kleinhammes, A.; Jia, Y.; Wu, Y.; Nguyen, S. T.; Ruoff, R. S. Synthesis of Graphene-Based Nanosheets *via* Chemical Reduction of Exfoliated Graphite Oxide. *Carbon* **2007**, *45*, 1558–1565.

59. Blakslee, O. L. Elastic Constants of Compression-Annealed Pyrolytic Graphite. *J. Appl. Phys.* **1970**, *41*, 3373.